Contributions of Interdecadal Pacific Oscillation and Atlantic Multidecadal Oscillation to Global Ocean Heat Content Distribution

ZEYUAN HU

Department of Atmosphere and Ocean Sciences, Peking University, Beijing, China

AIXUE HU

Climate and Global Dynamics Laboratory, National Center for Atmospheric Research, Boulder, Colorado

YONGYUN HU

Department of Atmosphere and Ocean Sciences, Peking University, Beijing, China

(Manuscript received 29 March 2017, in final form 27 October 2017)

ABSTRACT

Regional sea surface temperature (SST) mode variabilities, especially the La Niña–like Pacific Ocean temperature pattern known as the negative phase of the interdecadal Pacific oscillation (IPO) and the associated heat redistribution within the ocean, are the leading mechanisms explaining the recent global warming hiatus. Here version 1 of the Community Earth System Model (CESM) is used to examine how different phases of two leading decadal time scale SST modes, namely the IPO and the Atlantic multidecadal oscillation (AMO), contribute to heat redistribution in the global ocean in the absence of time-evolving external forcings. The results show that both the IPO and AMO contribute a similar magnitude to global mean surface temperature and ocean heat redistribution. Both modes contribute warmer surface temperature and higher upper ocean heat content in their positive phase, and the reverse in their negative phase. Regionally, patterns of ocean heat distribution in the upper few hundred meters of the tropical and subtropical Pacific Ocean depend highly on the IPO phase via the IPO-associated changes in the subtropical cell. In the Atlantic, ocean heat content is primarily associated with the state of the AMO. The interconnections between the IPO, AMO, and global ocean heat distribution are established through the atmospheric bridge and the Atlantic meridional overturning circulation. An in-phase variant of the IPO and AMO can lead to much higher surface temperatures and heat content changes than an out-of-phase variation. This result suggests that changes in the IPO and AMO are potentially capable of modulating externally forced SST and heat content trends.

1. Introduction

The rate of increase in global mean surface air temperature (GMST) slowed during the early 2000s despite the rapid increase of greenhouse gases (GHGs) (Fyfe et al. 2016; Yan et al. 2016; Lewandowsky et al. 2016). This slowdown, often called the ''global warming hiatus,'' can be clearly seen in GMST from several leading observational datasets (Fyfe et al. 2016), although earlier research identified some observational uncertainty (Karl et al. 2015). Multiple studies suggest that this slowdown is contributed mostly by internal climate variability in the context of anthropogenic global warming (e.g., Meehl et al. 2011, 2013b; England et al. 2014; Dai et al. 2015; Meehl et al. 2016), while changes in external forcing, such as volcanic activity (Santer et al. 2014) and aerosol forcing (Smith et al. 2016), may also play a role. The major internal climate mode variability associated with this slowdown is the interdecadal Pacific oscillation (IPO) (Zhang et al. 1997; Power et al. 1999; Meehl and Hu 2006). The anomalous SST cooling and strengthened trade winds in the eastern and central equatorial Pacific associated with the negative phase of the IPO have played a dominant role in producing the observed reduction in warming. Coupled global climate model simulations can successfully reproduce a reduced warming trend by restoring either sea surface temperatures (SSTs) (Kosaka and Xie 2013, 2016) or trade winds

Corresponding author: Aixue Hu, ahu@ucar.edu

DOI: 10.1175/JCLI-D-17-0204.1

(England et al. 2014) in the equatorial Pacific to the observations.

Moreover, this slowdown has spurred huge research interest in heat redistribution within the ocean. Observed energy imbalance at the top of the atmosphere (TOA) in the past few decades indicates a constant energy input of $\sim 1\,\mathrm{W\,m^{-2}}$ into Earth's climate system (Hansen et al. 2011; Trenberth et al. 2014) and the majority of this excess heat resides in the ocean (Palmer et al. 2011). However, how this added heat is distributed within the ocean is mostly determined by internal oceanic processes. These processes can either keep most of the heat gain in the surface ocean or deposit it into the subsurface or deep ocean. Many studies have tried to identify the heat redistribution pattern associated with the hiatus (Meehl et al. 2011; Chen and Tung 2014; Lee et al. 2015; Nieves et al. 2015; Liu et al. 2016a,b). For instance, Liu et al. (2016b) showed that the anomalous warming in subsurface Indian Ocean waters associated with strengthened heat transport from the Pacific through the Indonesian Throughflow is related to the recent warming slowdown. However, large uncertainties still exist with regard to the patterns of the observed heat redistribution due to lack of consistent observations and discrepancies among different observed datasets (Chen and Tung 2016; Liu et al. 2016a).

Here, we explore how modes of internal climate variability modulate oceanic processes and how they play a role in the redistribution of heat within the ocean under preindustrial external forcing conditions. In the process, we isolate the relationship between internal variability and changes to ocean heat content (OHC) without contamination from the time-evolving external forcing changes. In fact, the interplay between internal climate variability and external forcing is an active research topic and how this interplay affects the distribution of heat in the ocean will be our future focus.

The two modes of internal variability we are testing are the IPO and the Atlantic multidecadal oscillation (AMO). These major decadal and multidecadal time scale mode variabilities in the Pacific and Atlantic are identified by both observational and modeling studies (e.g., Power et al. 1999; Meehl and Hu 2006; Deser et al. 2010; Delworth and Mann 2000; Zhang and Delworth 2006, 2007). They can both influence global-scale climate phenomena, such as rainfall in East Asian (Si and Ding 2016) or drought in the southwestern United States (Meehl and Hu 2006). To investigate the contribution of the IPO and AMO to the redistribution of ocean heat, we use the preindustrial control, a member of the Community Earth System Model (CESM1 v1; Hurrell et al. 2013) Large Ensemble project (Kay et al. 2015). In our analysis, we focus on global mean OHC as well as OHC anomalies among ocean basins and subbasins of the Pacific and Atlantic to connect the OHC anomalies to underlying physical processes.

The physical mechanisms governing the IPO are still under intense debate due to a lack of reliable long-term observations and because of the complicated interactions among different components of the climate system. Currently, three primary mechanisms for governing the IPO have been proposed. The first theory asserts that the IPO represents a low-frequency response of the surface ocean to a stochastic atmospheric forcing (Hasselmann 1976; Frankignoul and Hasselmann 1977). A second theory posits that the IPO represents changes in SST due to advection in upper ocean circulation (Saravanan and McWilliams 1998; Meehl et al. 1998), oceanic gyre dynamics (Dewar 2001; Hogg et al. 2005; Taguchi et al. 2005; Ceballos et al. 2009), and oceanic Rossby wave adjustment (Qiu 2003; Schneider and Cornuelle 2005; Qiu et al. 2007). The third potential mechanism is that the IPO represents an air–sea coupling process, such as the unstable air–sea interactions over the North Pacific (Latif and Barnett 1994, 1996).

Similarly, the driving mechanisms of the AMO are also poorly understood and under intense debate. There are also three major mechanisms that are theorized to explain the AMO. The first theory is that the AMO is governed by oceanic processes, principally the Atlantic meridional overturning circulation (AMOC). Changes in AMOC modulate oceanic meridional heat transport, thus affecting the North Atlantic SST (Delworth et al. 1993; Delworth and Mann 2000; Latif et al. 2004; Knight et al. 2005; Semenov et al. 2010; Gulev et al. 2013; McCarthy et al. 2015; Zhang et al. 2016). A second theory is that indirect effects of anthropogenic aerosols influence long-term SST variability in the Atlantic (Mann and Emanuel 2006; Booth et al. 2012; Evan et al. 2009). The third potential mechanism is that the AMO is simply an SST response to midlatitude atmospheric stochastic forcing (Clement et al. 2015). In this paper, we do not explore the mechanisms governing the IPO or AMO, but instead focus on the relationship between the IPO/AMO states and changes in OHC.

The remainder of this paper is organized as follows. In section 2 we describe the model and the experimental design used for the results we present in this paper. Section 3 compares the fidelity of the simulated the IPO and AMO with observations. Section 4 quantifies the contributions of the IPO and AMO to global and regional OHC distribution and discusses the potential interaction between the IPO and AMO. Discussions and conclusions are given in sections 5 and 6, respectively.

2. Model and experiment

The climate model used for this research is the Community Earth System Model, version 1 (CESM1; Hurrell et al. 2013) with nominal 1° horizontal resolution for all components. The atmospheric component is the Community Atmosphere Model, version 5 (CAM5); the ocean component is the Parallel Ocean Program, version 2 (POP2); the land component is the Community Land Model, version 4 (CLM4), and the sea ice model is the Community Sea Ice Code, version 4 (CICE4). The twentieth-century climate simulated by CESM1 agrees reasonably well with observations (Meehl et al. 2013a).

This paper leverages a fully coupled 2200-yr preindustrial (PI) control simulation from the CESM Large Ensemble (CESM_LE; Kay et al. 2015). We use the PI control because our focus is to assess the contribution of various modes of internal variability to the redistribution of oceanic heat in the absence of anthropogenic external forcing. We limit our analysis to the last 1000 years of the PI control to avoid including nonlinear trends in the deep ocean in our results. The small trend in deep ocean temperature after year 1200 is linear and we remove it from OHC analysis. Notably, this trend has minimal effect on the upper ocean; using the full 2200-yr control did not make a significant difference for the upper ocean. The observed SST data used for this analysis is the Hadley Center reconstructed ocean surface temperature dataset, HadISST1, from 1870 to 2014 (Rayner et al. 2003). All analyses hereafter are based on the detrended annual mean data.

Although the CESM1 can simulate twentieth-century observed climate reasonably well (Meehl et al. 2013a), certain biases still exist (e.g., Bryan et al. 2007; Danabasoglu 2008; Danabasoglu et al. 2012a,b; Neale et al. 2013). Using the 1° horizontal resolution POP2 ocean model, CESM1 does not adequately separate the Gulf Stream from Cape Hatteras; as a result, the location of the North Atlantic current is zonally biased (Weese and Bryan 2006). However, studies show that, in general, these biases affect the simulations quantitatively but do not fundamentally change the basic physical processes. Results discussed later in this paper, however, may be affected by these biases, so a multimodel approach may be needed in future work.

There are two terms which are used later in this study: heat content and heat density of seawater. The heat content of seawater is defined as

$$\mathrm{HC} = \iiint \rho \mathrm{Cp} T \, dx \, dy \, dz, \tag{1}$$

where HC represents heat content, ρ is the potential density of seawater, Cp is the specific heat of seawater, T is the potential temperature of seawater, and dx, dy, and dz represent the width of a model grid in the zonal, meridional, and vertical directions. The heat density of seawater is defined as

$$\mathrm{HCD} = \frac{\iiint \rho \mathrm{Cp} T \, dx \, dy \, dz}{\iint dx \, dy}, \tag{2}$$

where HCD represents heat density.

3. Simulated and observed IPO and AMO

a. A comparison of observed and modeled IPO

The IPO pattern is defined as the first mode of the empirical orthogonal function (EOF) analysis on low-pass filtered (13-yr cutoff) and detrended Pacific SST (40°S–65°N, 110°E–75°W) for both observed and simulated data (Power et al. 1999; Meehl and Hu 2006). The IPO index is defined as the normalized time series of the first principal component (PC) (Fig. 1a and 1b; blue lines). The observed and modeled IPO indices explain a similar percentage of the SST variance (34.9% and 35.9%, respectively) in the Pacific. The observed IPO shows spectral peaks at 12–25 years (Fig. 1c) in our analysis and ~50 years from another study (Deser et al. 2010). The simulated IPO spectrum has more peaks, such as at 13–20, 22–33, and ~50 years (Fig. 1f), which may be related to the fact that we are using a much longer modeled than observed time series (1000 vs 142 yr).

The regression patterns of SST anomalies and the normalized IPO index for both observations and model simulations are given in Figs. 2a and 2b (the IPO patterns). The pattern correlation between the modeled and observed IPO is 0.8 in the Pacific, but only 0.19 globally. This implies that the model captures the dominant signature of the IPO on observed SST in the Pacific, but was not able to reproduce the observed teleconnections. Potentially, these teleconnections could be reinforced or modulated by the time-evolving external forcings, such as anthropogenic greenhouse gases, which needs to be explored further. In the Indian Ocean, the observed positive IPO pattern of SST is characterized by a basinwide warm anomaly, whereas the modeled IPO shows a dipole pattern. In the Atlantic Ocean, both the modeled and observed IPO show, in general, warm SST anomalies over the equatorial and subtropical Atlantic regions for a positive IPO (correlation ranging from 0.2 to 0.6, which is similar to observed; figure not shown) with reduced agreement in regions north of 30°N. Notably, the seesaw pattern simulated by the model does not appear in the observations. In the

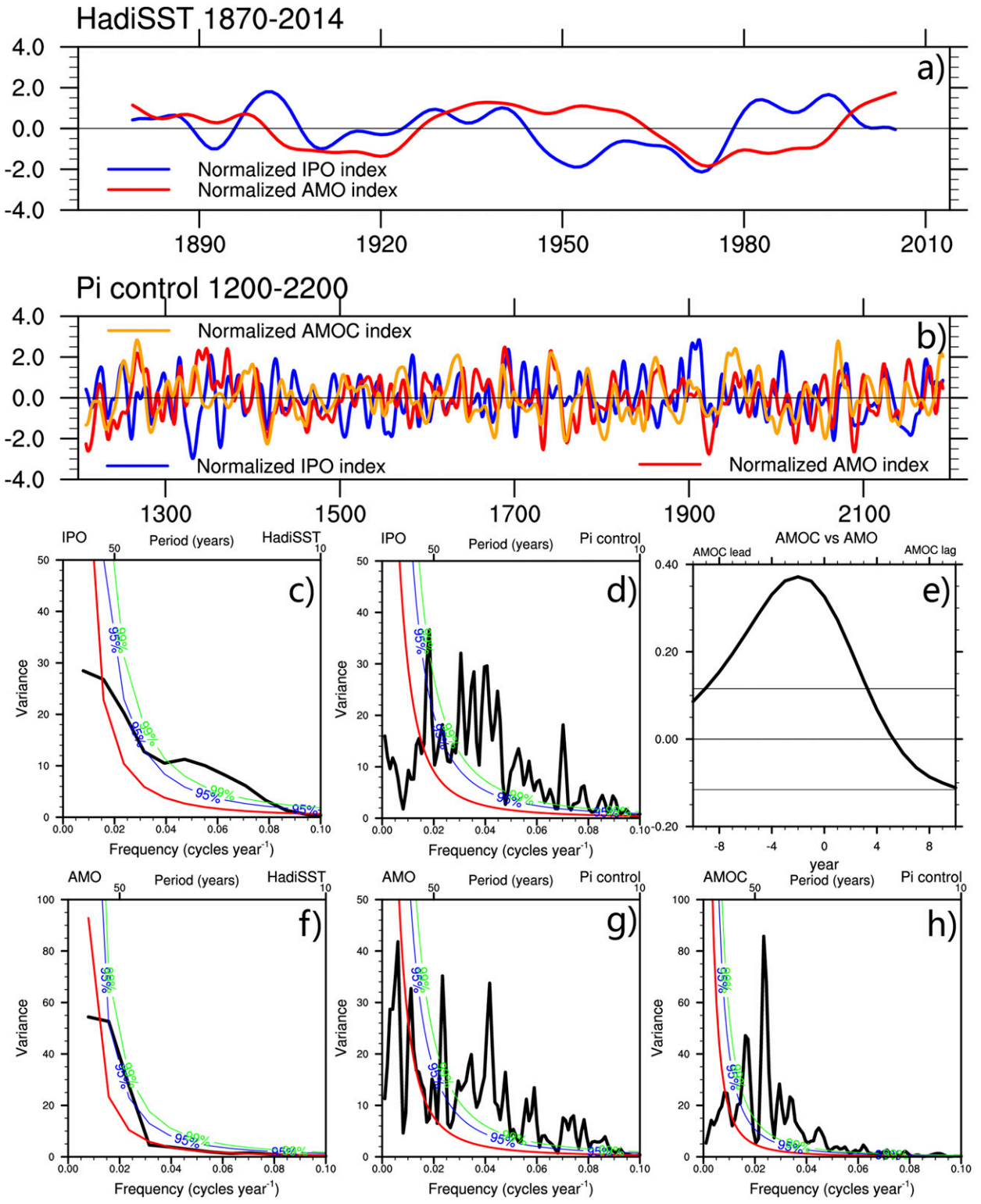

FIG. 1. Analysis of time series of IPO and AMO in observation and in CESM. (a) Observed IPO index (blue line) and AMO index (red line). (b) IPO index (blue line), AMO index (red line), and AMOC index (orange line) in CESM. (c) Observed power spectrum of IPO. (d) Observed power spectrum of AMO. e) Lead–lag correlation between AMO and AMOC. (f) Power spectrum of IPO in CESM. (g) Power spectrum of AMO in CESM. ((h) Power spectrum of AMOC in CESM. In (c), (d), (f), (g), and (h), the red line indicates the ''red noise'' curve, and the blue and green lines indicate the 95% and 99% significance levels.

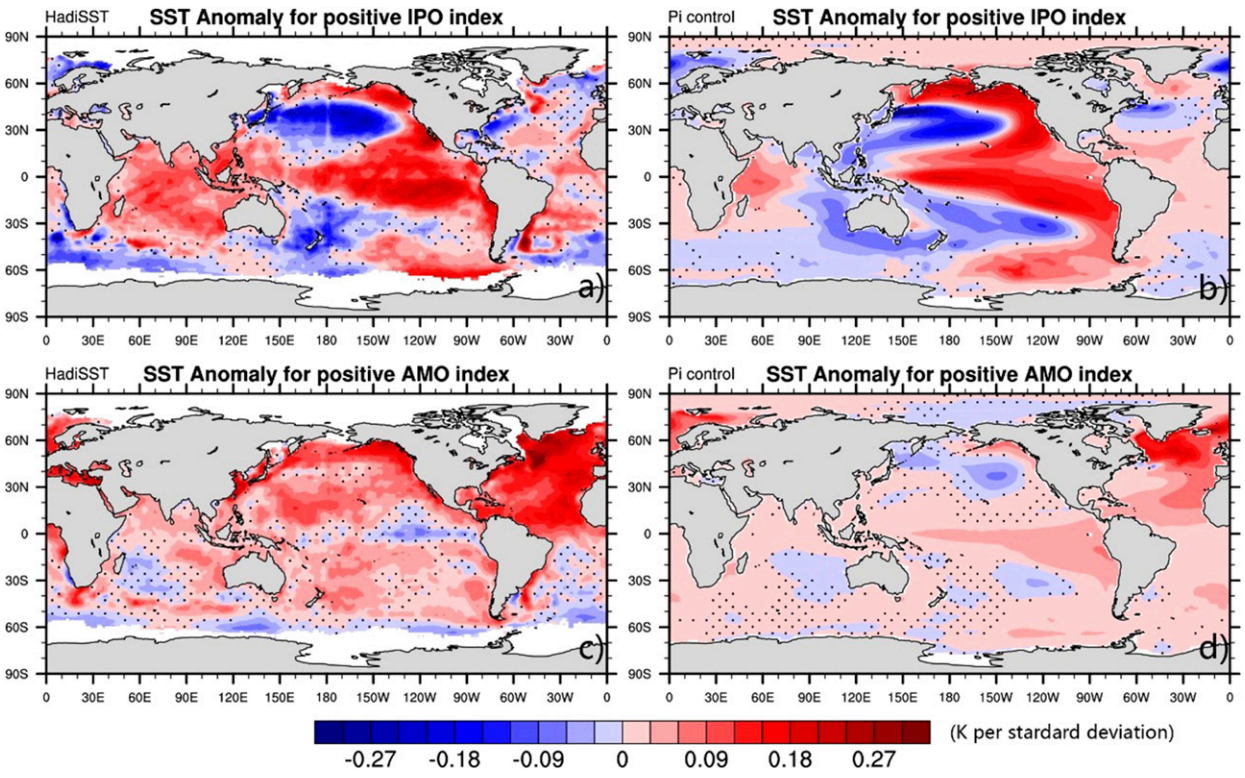

FIG. 2. Regression of normalized indices of the (top) IPO and (bottom) AMO on annual mean SSTs from (left) observations and (right) the CESM preindustrial control run. Stippling indicates regions below 95% significance.

Southern Ocean, both modeled and observed IPO patterns shows positive SST anomalies for positive IPO over the middle to eastern sections of the Pacific and negative SST anomalies for other sectors. Overall, the model reproduces the observed IPO spatial patterns and frequencies reasonably well, especially in the Pacific basin.

b. Comparing the observed and modeled AMO

Here, the AMO index is defined as the detrended and low-pass filtered SST anomaly averaged over the entire North Atlantic basin (0°–70°N, e.g., Kaplan et al. 1998; Buckley and Marshall 2016). A linear trend is removed from the data and a Lanczos low-pass filter (13-yr cutoff) is applied to the area-weighted mean SST to derive the AMO index as shown in Fig. 1a for observations and Fig. 1b for model simulations (red lines). The observed AMO has a significant spectral peak at ~60 years (Fig. 1d), agreeing with previous studies (e.g., Buckley and Marshall 2016). The most significant spectrum peaks for the modeled AMO are 25 and 40 years, with some other minor peaks ranging from decadal to multidecadal. Thus, the longest significant period for the modeled AMO is a bit shorter than for the observed. Besides the difference in data length, anthropogenic external forcing may also contribute to spectral differences between the modeled and observed AMO (e.g., Booth et al. 2012; Si and Hu 2017).

The regression patterns of the normalized AMO and SST anomalies are shown for observations (Fig. 2c) and for the model (Fig. 2d). The pattern correlation between modeled and observed AMO patterns is 0.75 in the Atlantic basin, but only 0.19 globally. The low global pattern correlation between modeled and observed AMO arises primarily from the Pacific and Indian Oceans, suggesting that the teleconnections between the North Atlantic and other ocean basins are not well simulated in CESM1. In general, the modeled AMO captures the major features of the observed AMO in the Atlantic basin with much reduced impact on SST, as demonstrated by smaller regression coefficients. Therefore, although the relationship between the AMO and Atlantic SST may be well simulated by the model, the global influence of the AMO on SST is not well reproduced by CESM1, due in part to the lack of the time-evolving external forcings.

c. Relationship of modeled AMO and AMOC

Usually, the AMO is considered to be governed by both AMOC, an internal ocean process (Delworth and

TABLE 1. Composite average in different phases of IPO and AMO. The CL mean index is the climatological mean of the corresponding index in its corresponding phase; "Mean index" is the mean index value for the composite analysis, which is the mean of the corresponding index greater than 1 (less than −1). By comparing these two mean indices, it shows that the mean index value for the composite analysis is about twice as much as that of the climatological mean index for each phase of the IPO or AMO. GMST represents the global mean surface temperature anomaly relative to the climatological mean; GM OHC represents the global mean ocean heat content anomaly relative to the climatological mean; Pac OHC is the mean ocean heat content in the Pacific basin north of 34°S; and Atl OHC is the mean ocean heat content in the Atlantic between roughly 80°N and 34°S. Also, (<100 m) represents the total OHC in the upper 100-m ocean,and (100–300 m) represents the total OHC in the ocean layer between 100- and 300-m depth. TheIPO/AMO index is unitless because these indices are standardized. The unit for GMST is °C. The unit for ocean heat content is 10^{21} J.

	IPO+	IPO−	AMO+	AMO−	IPO+ and AMO+	IPO− & AMO−
CL mean index	0.84	−0.76	0.82	−0.78		
Mean index	1.55	−1.50	1.49	−1.63	1.57/1.61	−1.33/−1.74
GMST	0.053 ± 0.012	−0.054 ± 0.012	0.040 ± 0.015	−0.049 ± 0.016	0.076 ± 0.027	−0.087 ± 0.032
GM OHC (<100 m)	3.21 ± 0.59	−3.04 ± 0.67	2.19 ± 0.60	−4.32 ± 0.70	3.80 ± 1.37	−6.26 ± 1.45
GM OHC (100–300 m)	−2.62 ± 0.69	−1.91 ± 0.85	1.59 ± 0.86	−2.42 ± 0.57	−1.73 ± 1.87	−2.96 ± 1.50
Pac OHC (<100 m)	2.72 ± 0.28	−2.76 ± 0.33	0.56 ± 0.34	−1.48 ± 0.40	2.05 ± 0.56	−3.00 ± 0.69
Pac OHC (100–300 m)	−2.29 ± 0.44	1.60 ± 0.57	0.65 ± 0.55	−0.63 ± 0.44	−2.85 ± 1.19	−0.78 ± 0.85
Atl OHC (<100 m)	0.50 ± 0.18	−0.30 ± 0.21	1.55 ± 0.12	−1.85 ± 0.13	2.14 ± 0.27	−2.29 ± 0.37
Atl OHC (100–300 m)	0.16 ± 0.18	0.16 ± 0.21	0.81 ± 0.18	−0.92 ± 0.20	1.33 ± 0.30	−0.85 ± 0.50

Mann 2000; Zhang and Delworth 2006; Zhang et al. 2016), and the combined effect of external atmospheric forcing and intrinsic variability (e.g., changes in aerosol forcing and the North Atlantic Oscillation) (Booth et al. 2012; Clement et al. 2015; Buckley and Marshall 2016). Because our analysis is focused on the preindustrial control simulation, we lack anthropogenic forcing and examine only the relationship between the AMO and AMOC. The AMOC index is defined as the maximum of the meridional overturning streamfunction below 500-m depth in the Atlantic Ocean (Fig. 1b). The correlation of the AMO index and the AMOC index reaches +0.36 when the AMOC leads the AMO by two years (Fig. 1e). The major spectrum peaks of the AMOC are a bit longer, such as ~60 and ~45 years, and there are also peaks for a shorter period ranging from less than 20 years to about 40 years. Moreover, many of the AMOC frequencies are in good agreement with those of the AMO (Figs. 1h,g). A separate study used the same data applies wavelet spectrum analysis and the cross-wavelet transform and wavelet coherence analyses, corroborating the covariance of the AMOC and the AMO in both wave power and relative phase domain (Si and Hu 2017). Therefore, the AMOC contributes significantly to the AMO variability in our simulation and agrees well with other investigations (e.g., Delworth and Mann 2000; Zhang and Delworth 2006; Zhang et al. 2016).

4. Decadal modes and OHC distribution

a. *Contributions of the IPO to global and regional OHC anomalies*

We use composite analysis to assess the contribution of different IPO or AMO mean states to the regional and global OHC changes. A composite positive IPO (IPO+) is defined as the ensemble mean of years with a normalized IPO index greater than 1 standard deviation, and a composite negative IPO (IPO−) is defined as the ensemble mean of years with the normalized IPO index less than −1 standard deviation. In this 1000-yr-long time series, there are 163 IPO+ years (with a mean IPO index of 1.55; roughly twice as large as the mean IPO index for all positive IPO years) and 155 IPO− years (with a mean IPO index of −1.50; Table 1). We follow this definition of the composite IPO+ or IPO− throughout the remainder of this paper and refer to the composite IPO+ (IPO−) as IPO+ (or IPO−).

The global mean OHC anomaly for an IPO+ and IPO− state relative to the climatological mean OHC in various ocean layers is given in Fig. 3a. In general, OHC anomalies in the upper 100 m are opposite to those at 100–300-m depths, and the OHC anomalies for an IPO+ phase are opposite to those for an IPO− phase. For example, OHC in the upper 100-m layer has a positive anomaly of 3.2×10^{21} J for an IPO+ state and the associated GMST anomaly is 0.053°C relative to the climatological mean (Table 1). But, the OHC in the 100–300-m layer has a negative anomaly (-2.6×10^{21} J), accounting for 82% of the positive OHC anomaly in the upper 100 m. The inverse relationship between the OHC anomaly at the surface to that at depths of 100–300 m implies that different phases of the IPO induce contrasting OHC anomalies in the upper few hundred meters of the ocean. For the IPO− phase, OHC anomalies for the upper 100-m (-3.0×10^{21} J) and 100–300-m ($+1.9 \times 10^{21}$ J) layers are also opposite in sign, with an associated GMST anomaly of −0.054°C (Table 1). Below 300 m, the sign of the OHC anomaly is generally

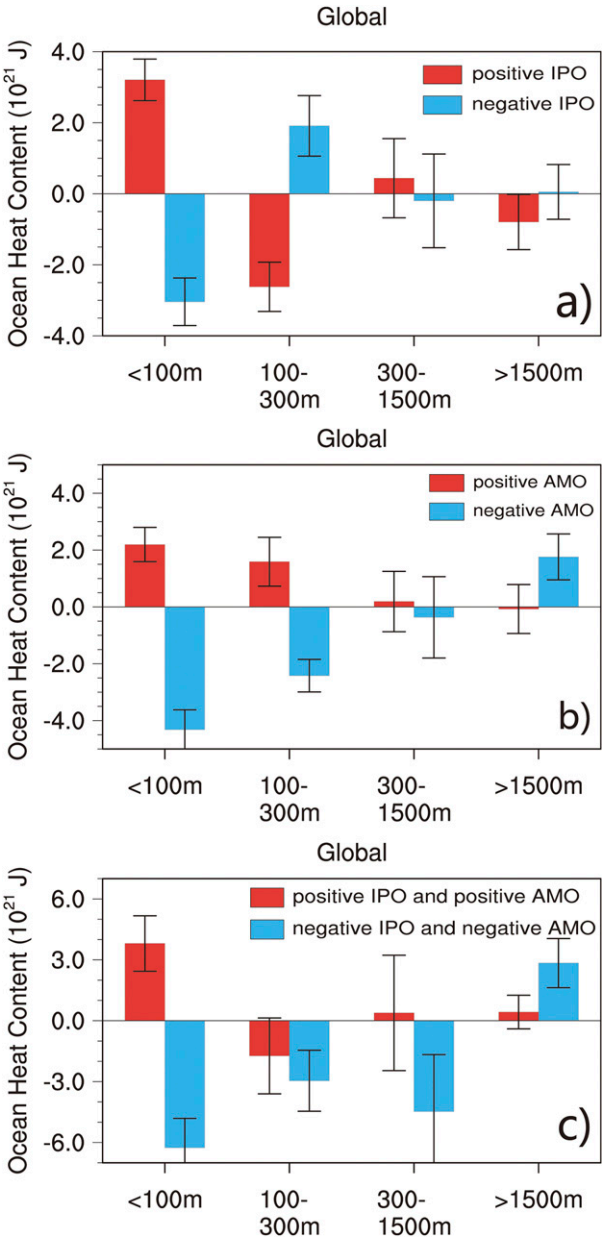

FIG. 3. Composite mean global OHC anomalies at different layers for different phases of the IPO and AMO, namely (a) the IPO, with, red (blue) bar for positive (negative) IPO; (b) the AMO, with red (blue) bar for positive (negative) AMO; and (c) in-phase IPO and AMO, with red (blue) bar for in-phase positive (negative) IPO and AMO. Error bars denote 95% confidence interval.

the same as for the subsurface layer (100–300 m) of the ocean, with an OHC increase for an IPO− phase, and a decrease for an IPO+ phase, while the magnitude of the anomaly is less significant.

The primary contributions to this pattern of global OHC anomaly associated with the IPO phase come from the Pacific Ocean (Fig. 4a and Table 1). For both the IPO+ and IPO− phases, the Pacific OHC anomalies in both the upper 100-m and 100–300-m layers account for over 85% of the global OHC anomalies. To explore this relationship, we divide the Pacific Ocean into different latitudinal bands in order to connect the underlying physical processes to the changes in OHC. These latitude bands are 1) the equatorial Pacific (15°S–15°N), 2) the subtropical and midlatitudinal South and North Pacific (34°–15°S and 15°–45°N), and 3) the subpolar North Pacific (45°–65°N). As shown in Figs. 4b–e, the upper 100-m OHC changes in the Pacific are dominated by the equatorial Pacific, accounting for 86% (76%) of the Pacific IPO+ (IPO−) OHC anomaly in the upper 100-m layer with the remainder coming from the subpolar North Pacific. In the subsurface layer (100–300 m), the contribution from the equatorial Pacific to the entire Pacific OHC anomaly is much smaller (a bit less than 40%) for both IPO+ and IPO−. On the other hand, the contribution from both the north and south subtropical and midlatitudinal regions to the upper 100-m layer Pacific OHC anomaly is minor, due in part to the opposite sign of the OHC anomaly in these two regions. In the subsurface layer (100–300 m), the OHC anomalies in both subtropical and midlatitudinal North and South Pacific are the same sign as the equatorial Pacific, and account for about 80% of the total Pacific OHC anomaly in this layer, but a portion of this anomaly is offset by the subpolar North Pacific.

The vertical distribution of the OHC anomaly in the Pacific can be understood more clearly by looking at the zonal mean ocean heat density, defined as the area-weighted mean OHC [J m^{-2}; see section 2, Eq. (2)], between the IPO+ and IPO− (Fig. 4f). In the equatorial region (roughly 27°S–27°N), there is a positive heat density anomaly for the upper 100 m, but a negative anomaly in regions between 27° and 45°N and between 34° and 27°S in the Pacific. An examination of the heat density anomaly also explains why OHC anomalies in the subtropical north and South Pacific remain small in the upper 100-m layer due in part to the effect of averaging both positive and negative anomalies in these two regions (34°–15°S and 15°–45°N). In the 100–300-m layer, the heat density anomaly is primarily negative with the exception of a few small regions. In the subpolar North Pacific, the heat density anomaly is the same sign to at least 700 m, consistent with Fig. 4b.

The pattern of OHC distribution described above in the equatorial and subtropical Pacific can be explained by changes in subtropical cells (STCs) in association with the IPO (Figs. 4g,h). STCs are shallow meridional overturning cells in the ocean on each side of the equator that extend to depths of roughly 700 m (e.g., McPhaden and Zhang 2002; Meehl and Hu 2006; Meehl

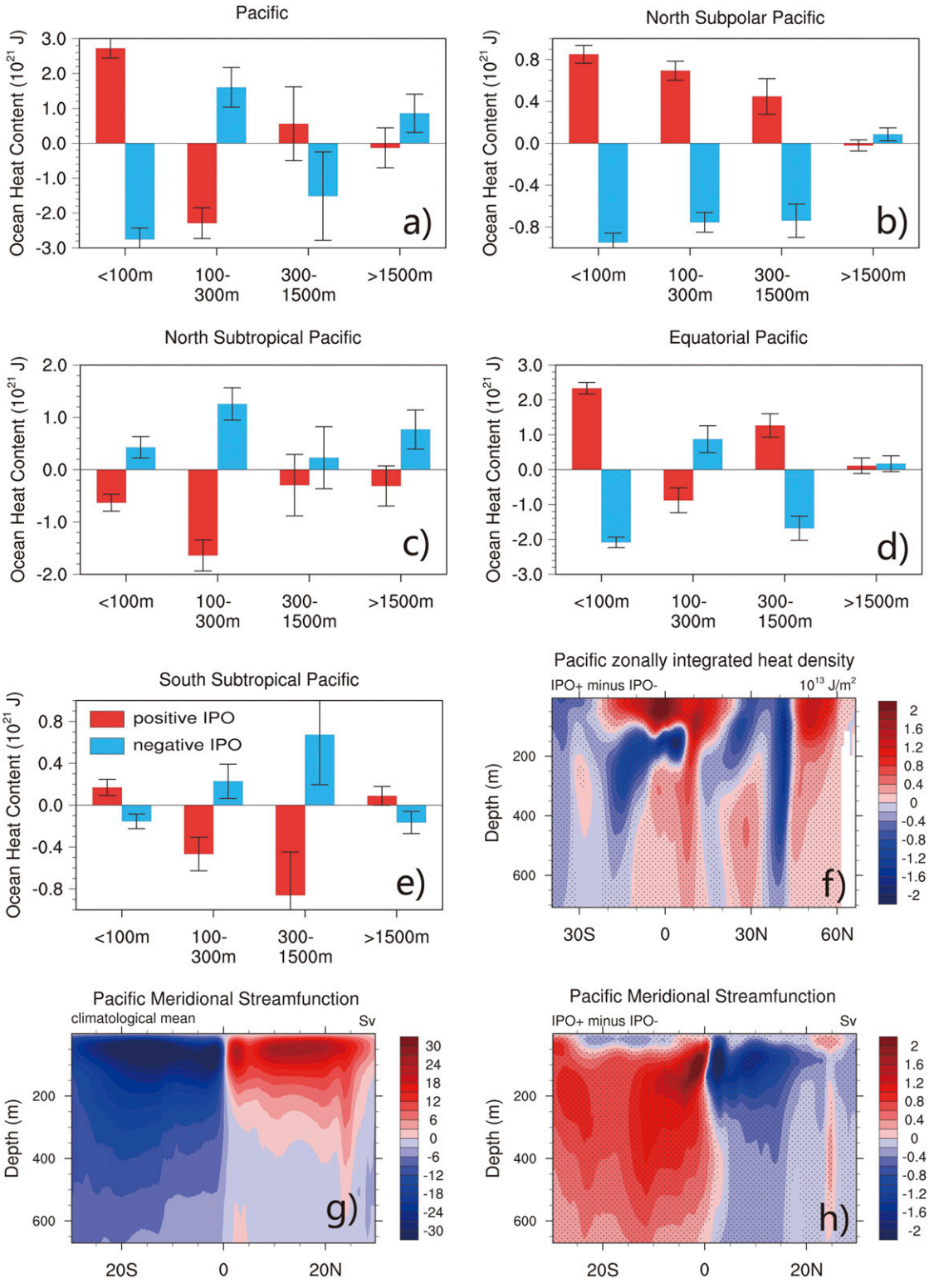

FIG. 4. Composite mean OHC anomalies for IPO+ and IPO− in the Pacific and its subbasins: (a) entire Pacific, (b) subpolar North Pacific, (c) subtropical North Pacific, (d) equatorial Pacific, and (e) subtropical South Pacific. Red bars represent OHC anomaly for IPO+ and blue bars represent OHC anomaly for IPO−. (f)–(h) The zonally integrated heat density anomaly between IPO+ and IPO−, climatological mean Pacific meridional streamfunction representing STCs, and the Pacific meridional streamfunction anomaly between IPO+ and IPO−, respectively. Error bars in (a)–(e) denote 95% confidence interval. Stippling in (f) and (h) indicates statistically significant changes. Sv represents units of Sverdrups, a volume transport in oceanography (10^6 m^3 s^{-1}).

et al. 2013b). During a positive phase of the IPO, the SST contrast between eastern and western equatorial Pacific weakens, leading to weakened equatorial easterlies (cf. Figs. 5a and 5b), with consequently weaker equatorial Ekman upwelling and weaker STCs (cf. Figs. 4g and 4h). These weaker STCs bring less colder subsurface water to the surface, resulting in a warmer equatorial upper ocean and increased OHC. Meanwhile, associated with weaker easterlies and westerlies induced by the positive IPO in the Pacific (Fig. 5b), the Ekman convergence in the subtropics weakens, along with a reduced downwelling there. As a result, less warm surface water is subducted, leading to a cooling of subsurface layers and a negative OHC anomaly in the subtropical regions. In the subpolar North Pacific, the OHC changes are linked to a weakened (strengthened) surface Ekman divergence related to the positive (negative) IPO-induced weakening (strengthening) of the westerlies (Fig. 5b), and thus a weakened (strengthened) upwelling in this region.

The IPO contributes to ocean heat redistribution not only in the Pacific, but also in other ocean basins. However, correlated changes in OHC are less significant in other basins, possibly related to the weakly simulated IPO teleconnections in CESM. The climatological heat density (Fig. 6a) of the upper 100 m resembles the SST pattern. The heat density anomaly between the IPO+ and IPO− for this layer (Fig. 6b) resembles the regression pattern of the IPO and SST (Fig. 2b). Compared to the heat density anomaly in the Pacific, the anomaly in other basins is less than 50% of that seen in the Pacific. In the eastern Indian Ocean, the heat density anomaly has the same sign as in the western Pacific, suggesting an influence of the Pacific on the Indian Ocean, potentially by way of the Indonesian Throughflow (Liu et al. 2016b). In the Pacific sector of the Southern Ocean, the heat density anomaly is positive (or negative if this anomaly is defined as IPO− minus IPO+). Meehl et al. (2016) suggest the negative IPO has contributed to the recent sea ice expansion in the Pacific sector of the Southern Ocean. Our analysis indicates that the negative OHC anomaly in the same sector during the IPO− in recent hiatus years along with strengthened westerlies (Fig. 5b) may have also contributed to sea ice expansion there.

b. *The AMO contributions to global and regional OHC anomaly*

Analogous to the IPO, a composite positive AMO (AMO+) is defined as the ensemble mean of years with a normalized AMO index greater than 1, and a composite negative AMO (AMO−) is defined as the ensemble mean of the years with a normalized AMO index less than −1. There are 159 sample years that meet the AMO+ definition in the 1000-yr-long control run, with a mean AMO index of 1.49, and 135 AMO− sample years with a mean AMO index of −1.63. We adhere to these definitions for the remainder of the text and refer the composite AMO+ (AMO−) as AMO+ (AMO−).

Figure 3b shows the global mean OHC distribution at different layers for the AMO+ and AMO− phases. In contrast to the IPO, the OHC anomalies in the upper 100-m and 100–300-m layers are of the same sign. Moreover, there is a significant asymmetry in the OHC anomaly for the AMO− (-6.7×10^{21}J), when compared to the anomaly for the AMO+ (3.8×10^{21} J; Table 1). The OHC anomaly for the AMO− is roughly twice that of the AMO+. The difference in corresponding GMST changes is much smaller (0.040°C for AMO+ vs −0.049°C for AMO−; Table 1). Changes in OHC in deeper layers are small, with the exception of the 1500-m layer for the negative AMO.

Regionally, the Atlantic Ocean contributes a significant portion of the AMO-related global OHC anomaly in the upper 300 m (Fig. 7a), but the asymmetry of the OHC changes in this layer between AMO+ and AMO− is mainly from the Pacific and Southern Oceans (figure not shown). The Atlantic OHC anomaly in the upper 300 m accounts for about 63% ($+2.4 \times 10^{21}$ J) of the global mean OHC anomaly in this layer for the AMO+, but 41% (-2.8×10^{21} J) of the global OHC anomaly in this layer for the AMO−. In the Pacific Ocean, the OHC anomaly in the upper 300 m contributes 32% ($+1.2 \times 10^{21}$ J) of the total OHC anomaly for the AMO+, and a similar percentage (32%, or -2.1×10^{21} J) for the AMO−. In the Southern Ocean, the OHC anomaly in the upper 300 m is small for the AMO+ but reaches 22% (-1.5×10^{21} J) for the AMO−. Thus, all ocean basins contribute to the global OHC anomalies for both the AMO+ and AMO− although the contribution from the Atlantic is larger than from other ocean basins. In deeper ocean layers, the OHC changes are less significant, except for in the Southern and Atlantic Oceans (figure not shown). These changes in OHC may not be directly related to the AMO; rather, they may be a delayed response to surface changes. The OHC changes in these layers generally have opposite signs between the AMO+ and AMO−.

Similar to our investigation of the Pacific, we divide the Atlantic into four subbasins, namely 1) the subpolar North Atlantic (45°–80°N), 2) the subtropical North Atlantic (45°–15°N), 3) the subtropical South Atlantic (15°–34°S), and 4) the equatorial Atlantic (15°S–15°N).

Depth-related changes in OHC in the Atlantic vary by latitude and are associated with different physical

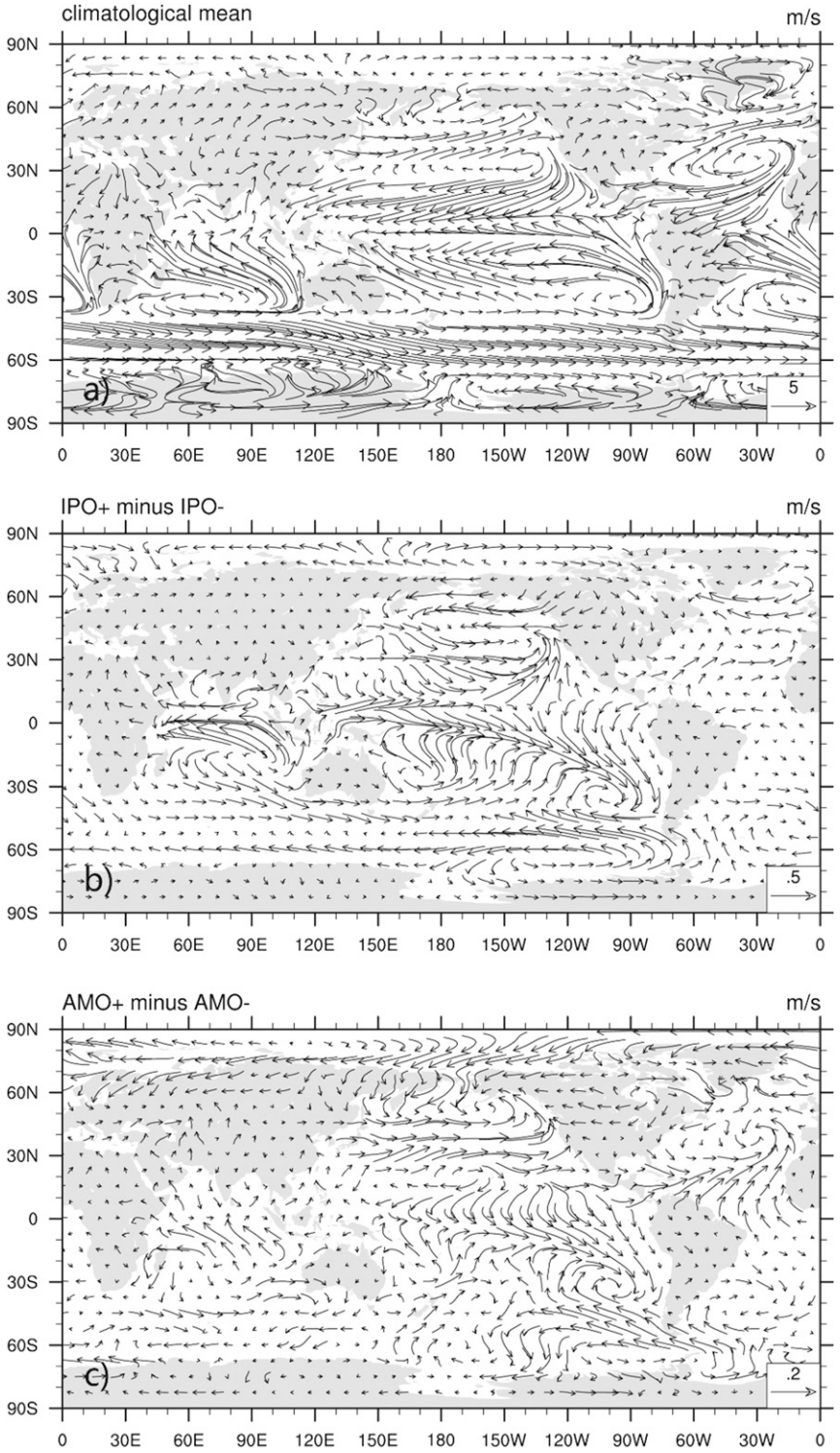

FIG. 5. (a) Climatological mean surface wind, (b) mean wind anomaly between positive and negative IPO, and (c) the mean wind anomaly between positive and negative AMO.

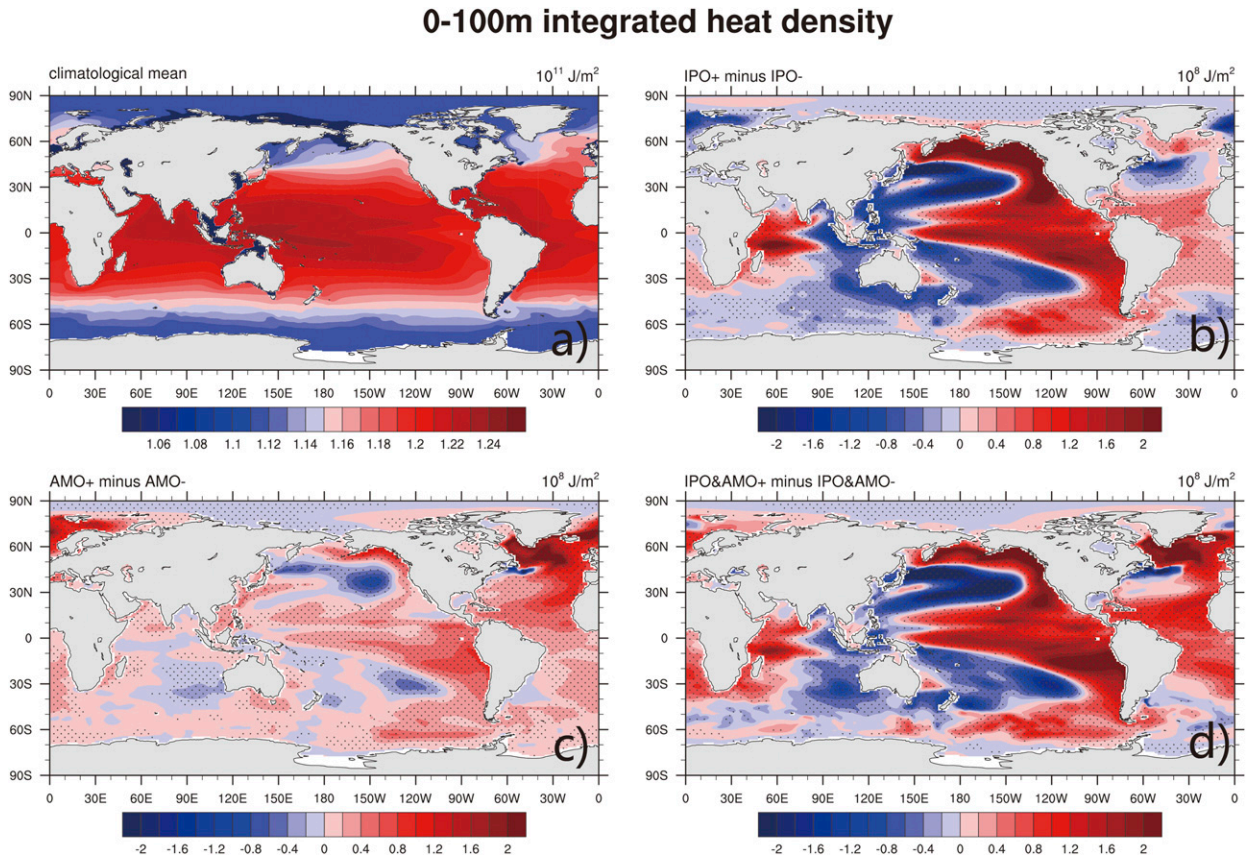

FIG. 6. Vertically integrated heat density defined as the vertically integrated heat content divided by the area of a given grid cell. (a) The climatological mean. Also shown are the heat density anomalies between (b) IPO+ and IPO−, (c) AMO+ and AMO− (c), and (d) IPO_AMO+ and IPO_AMO−. The unit is 10^6 J m^{-2}. Stippling indicates statistically significant changes at 95% level.

processes. For example, in the subpolar North Atlantic (Figs. 7b,f), the OHC anomaly carries the same signature from the surface to 1500 m for both the AMO+ ($+3.5 \times 10^{21}$ J) and the AMO− (-3.6×10^{21} J) (Fig. 7f). This OHC anomaly is related directly to changes in the AMOC strength and associated deep convection in the subpolar North Atlantic (Figs. 1e and 7g,h). One consequence of a change in the AMOC is an increase (decrease) in the corresponding meridional heat transport, leading to a positive (negative) OHC anomaly for the AMO+ (AMO−) in this region.

The OHC anomaly in the subtropical and tropical Atlantic has the opposite sign between the upper 100 m and the subsurface (100–300 m) layer. This relationship can be seen even more clearly in the zonal mean heat density anomaly between the AMO+ and AMO− (Fig. 7f). This pattern in OHC is associated with weak subtropical cells in the Atlantic. Although it is not very distinct, one still can see weak Atlantic STCs (Fig. 7g) and their associated changes (Fig. 7h). The latter panel suggests weaker STCs for the AMO+ than for the AMO−. Weak STCs reduce the downwelling of warm subtropical water, resulting in a relative cooling of the 100–300-m layer. Actually, the heat density anomaly between the AMO+ and AMO− in the upper 100 m shows a pattern that is similar to that seen in the Pacific between the IPO+ and IPO−, but with a reduced magnitude. Horizontally, the negative heat density anomaly only appears in a small portion of the west subtropical Atlantic on both hemispheres (Fig. 6c). As shown in Fig. 5c, the weaker STCs for the AMO+ are also related to the decrease of the easterly winds.

For ocean basins outside of the Atlantic, the simulated OHC response to the AMO has much larger uncertainty not only for the deep ocean, but also for the upper 300-m layer (figure not shown). For example, in the Indian Ocean the OHC anomalies between the AMO+ and AMO− are not significantly different from each other (e.g., $-0.10 \pm 0.10 \times 10^{21}$ J for the AMO+ vs $-0.22 \pm 0.10 \times 10^{21}$ J for the AMO− in the upper 100-m layer; $-0.07 \pm 0.22 \times 10^{21}$ J for the AMO+ vs $-0.07 \pm 0.22 \times 10^{21}$ J for the AMO− in the 100–300-m layer). The Pacific has a positive OHC anomaly in the upper 300-m layer for the AMO+ (1.21×10^{21} J) and a negative

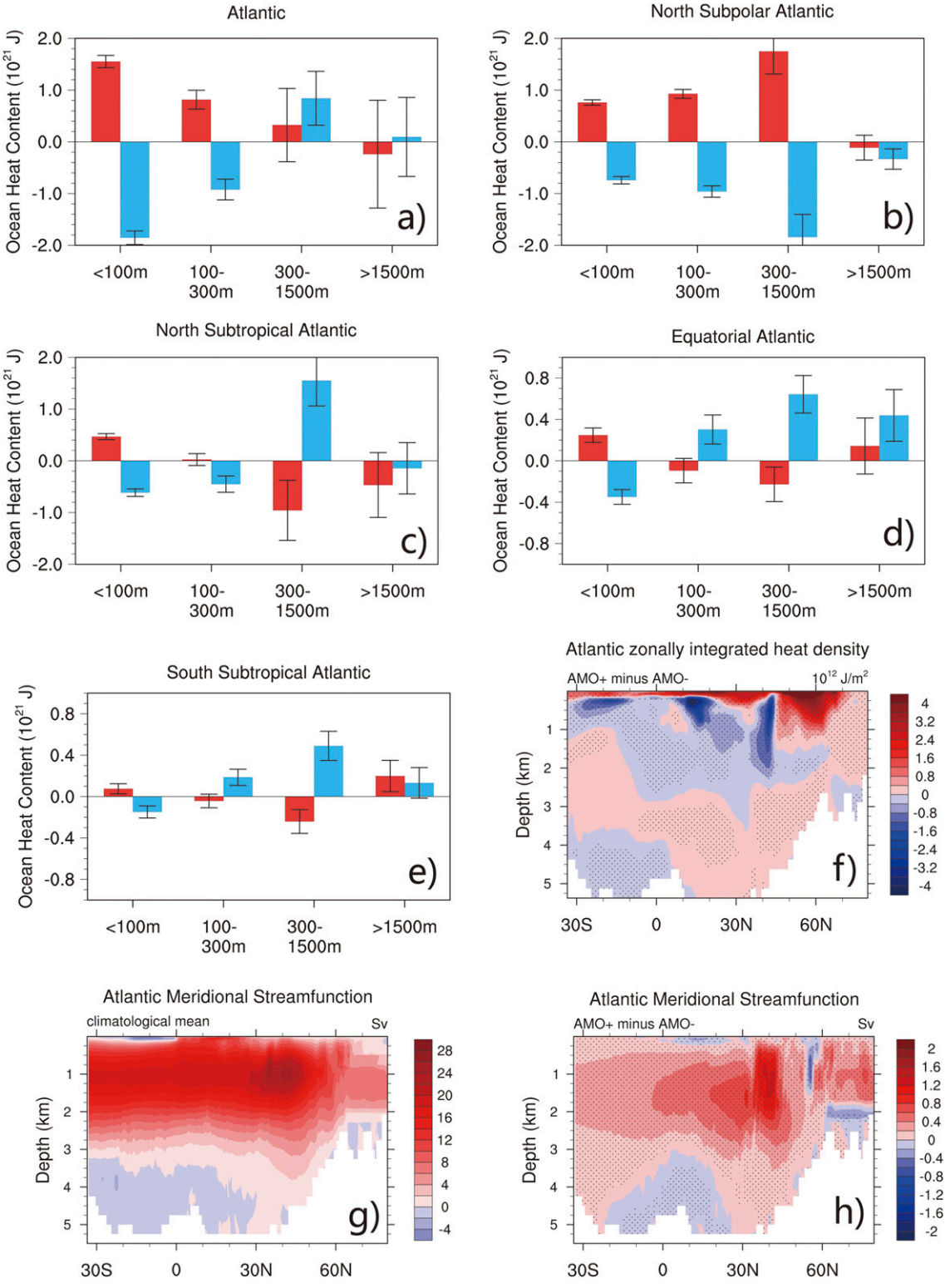

FIG. 7. As in Fig. 4, but for the AMO.

anomaly for the AMO− (-2.11×10^{21} J). There is a similar OHC anomaly in the Southern Ocean for this layer, although the OHC anomaly is much larger in the AMO− (-1.46×10^{21} J) than in the AMO+ (0.33×10^{21} J).

c. *OHC and synchronous phases of the IPO and AMO*

The IPO and AMO may not be independent from each other. Here we investigate further contributions of synchronous phases of the IPO and AMO to global and regional OHC changes. Previous studies suggest that the AMO may drive IPO variability in the Pacific (McGregor et al. 2014; Zhang and Delworth 2007). Thus, the influence on OHC of the coincident or "in-phase" IPO and AMO may differ significantly from that of either the IPO or the AMO acting alone. We filtered the 1000-yr-long control run for years where either the IPO or the AMO was in the positive phase (normalized IPO or AMO index greater than 1); in roughly 11% of these years, the alternate index (IPO or AMO) was also in phase. We also screened for years where either the IPO or the AMO was negative (normalized IPO or AMO index less than −1); in roughly 9.4% of these years the alternate index (IPO or AMO) was also in phase. Of these in-phase years, 32 years had both the IPO and AMO in their positive phase (normalized IPO and AMO indices both greater than 1; hereafter IPO_AMO+ years), and in 25 of these years the IPO and the AMO are both in their negative phase (normalized IPO and AMO indices both less than −1; hereafter IPO_AMO− years).

Figure 3c shows global mean OHC anomaly distribution by depth for the climatological mean of the IPO_AMO+ and IPO_AMO− years. OHC anomalies for in-phase years are, in general, larger than in years when the IPO or AMO is acting alone (Figs. 3a–c). For the IPO_AMO+ years, the global mean OHC anomaly in the 100-m layer is $+3.8 \times 10^{21}$ J (Fig. 3c), with a GMST anomaly of +0.076 K (Table 1). For the IPO_AMO− years, the 100-m layer anomaly is -6.3×10^{21} J (Fig. 3c), with a GMST anomaly of −0.087 K (Table 1). Contributions to this global mean OHC anomaly for the in-phase IPO and AMO come primarily from the Pacific and Atlantic Oceans. For the IPO_AMO+, roughly 50% of the OHC anomaly is contributed by the Pacific and the remainder comes from the Atlantic (Table 1). For the IPO_AMO−, roughly 50% of the OHC anomaly is coming from the Pacific, 36% from the Atlantic, and the remainder primarily from the Southern Ocean.

The change in OHC in the subsurface (100–300 m) layer for the IPO_AMO+ and IPO_AMO− years shows features that are distinctly different from years where either of the two modes is acting alone. These differences may reflect the interaction between the two modes and the underlying physical processes that drive them. The OHC anomalies in this layer are negative for both the IPO_AMO+ and IPO_AMO− years (Fig. 3c) and contributions to these anomalies come primarily from the Pacific and Atlantic basins (Figs. 8a,b). For the IPO_AMO+ years, the negative OHC anomaly in the Pacific is larger than the positive OHC anomaly in the Atlantic, resulting in an overall negative OHC anomaly. For the IPO_AMO− years, both the Pacific and Atlantic basins have negative OHC anomalies. However, the negative anomaly in the Pacific is insignificant (Fig. 8a, Table 1) and is mostly from the subpolar North Pacific with some contribution from the equatorial and subtropical South Pacific (Figs. 8c,e,g,i). The negative OHC anomaly in the Pacific for the IPO_AMO+ years comes primarily from the subtropical North Pacific with some contribution from the equatorial and subtropical South Pacific, which is a bit different from the IPO+ case. In the Atlantic, the OHC anomalies for both the IPO_AMO+ and IPO_AMO− are mostly from the subpolar North Atlantic with small contributions from other parts of the Atlantic (Figs. 8b,d,f,h,j). This implies that changes in deep convection may play a dominant role in determining the sign of the OHC anomaly in the Atlantic. In fact, by comparing Figs. 7a–e with the right panels in Fig. 8, one can see significant similarities, which suggests that the contribution of the IPO to Atlantic OHC anomaly is very small in the CESM1 control simulation. Conversely, the contribution from the AMO to Pacific OHC is significant (Figs. 4a–e and 8, left panels) and appears to be related to the AMOC and the associated changes in meridional heat transport (e.g., Hu et al. 2010, 2011, 2012, 2015). For example, when AMOC weakens, northward meridional heat transport in the Atlantic basin decreases. Simultaneously, the meridional heat transport in the Pacific also changes; northward heat transport from the equatorial Pacific to the subpolar North Pacific increases, but the southward heat transport from the equatorial Pacific to the South Pacific declines. Because the AMO is heavily affected by the AMOC in the control simulation (Si and Hu 2017), changes in meridional heat transport in different ocean basins in association with the AMOC further affect the change in ocean heat content in the Pacific (Figs. 4a–e).

Overall, the OHC anomaly in the upper 100-m layer shows consistent change that can be correlated with the IPO in the Pacific and with the AMO in the Atlantic, suggesting the dominance of these modes within their own basins. The slight contribution of the IPO to OHC in the upper 100-m layer in the Atlantic shows that it does not play a dominant role. The same is true for the effect of the AMO on the upper 100-m layer in the Pacific.

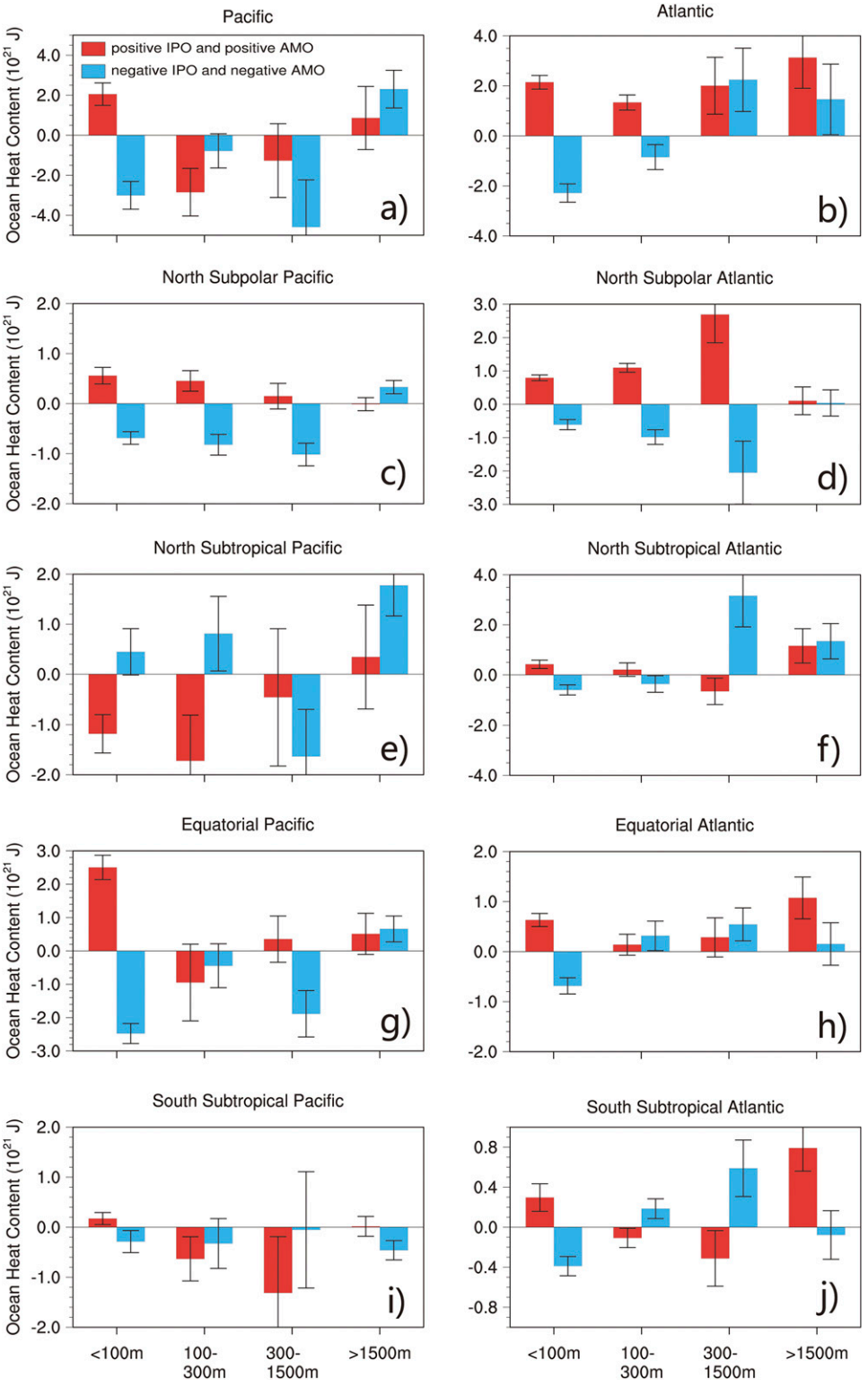

FIG. 8. As in Figs. 4a–e, but for in-phase IPO and AMO. Red (blue) bars denote in-phase IPO_AMO+ (IPO_AMO−).

For the subsurface layer (100–300 m), the OHC anomalies in the subpolar North Pacific and North Atlantic are consistent with those of IPO or AMO acting alone in their own basin, but for other regions, changes in OHC in response to the in-phase IPO_AMO+/IPO_AMO− are distinct from the effect of either the IPO or AMO acting alone. These differences are likely due to changes in subsurface ocean circulation associated with variations in the AMOC. Given the time lag in the response of OHC to changes of the AMOC, the timing of the IPO_AMO+ or IPO_AMO− years may not coincide with the peak of positive/negative IPO or AMO, leading to differences in the OHC response to the IPO and AMO.

5. Discussion

In general, the CESM1 control simulation captures the main features of the observed IPO spatial pattern and time series spectrum, with peaks at 20–30 years and ~50 years. The modeled AMO spatial pattern is also in good agreement with observations, and the AMO has a peak spectrum at ~45 years, which is a bit shorter than seen in observations (~60 yr) but consistent with the peak spectrum of AMOC in our model. The latter indicates that the AMOC plays a central role in modulating the AMO in the absence of time-evolving external forcing, since the lead–lag correlation shows that the AMOC leads the AMO by two years. However, the spatial pattern of the simulated IPO or AMO in ocean basins other than the Pacific or Atlantic does not agree with observations, implying 1) that the teleconnections via atmospheric or oceanic processes may not be simulated well in the CESM or 2) that external forcing may modify the teleconnection pattern (Si and Hu 2017).

On decadal time scales, the contribution of the IPO to global OHC distribution is primarily to the upper 300-m layer, and the contribution to deeper layers is less significant, with the exception of the subpolar North Pacific. This is related to the fact that it takes time to propagate surface changes into the deep ocean, especially since deep ocean convection only occurs in selected subpolar regions where there is much more rapid communication between the upper and deeper ocean. The composites for the IPO+ and IPO− are based on the integrated model data from the full water column, and the time lag for the changes to propagate from top to bottom is not considered here. Under the IPO+ (IPO−), the dominant feature in the upper 300 m is the opposing sign of OHC anomalies between the upper 100-m layer and the 100–300-m layer, outside of the subpolar region where the sign of the OHC anomaly is consistent between these two layers. This pattern of OHC anomaly is related to the changes in subtropical cells associated with different IPO phases (McPhaden and Zhang 2002; Meehl and Hu 2006). In other ocean basins, the OHC anomalies are less significant, implying a small contribution from the IPO.

The contributions of the AMO to the global-mean upper 100-m OHC and GMST are on the same order of magnitude as those of the IPO. In the Atlantic Ocean, there is a basinwide increase in OHC under the AMO+ and a decrease under the AMO− in the upper 100-m layer. This pattern of change in OHC agrees well with the regression pattern of the AMO and SST (Fig. 1d). Under the AMO+, a stronger positive OHC anomaly appears in the subpolar North Atlantic in the upper 1500 m resulting from a strengthened AMOC. In the subtropical and equatorial Atlantic, the positive OHC anomalies in the upper 100-m layer and the negative OHC anomalies in the 100–300-m layer are associated with both the Atlantic STCs and the AMOC. Outside the Atlantic basin, the contribution of the AMO to OHC anomalies are less significant.

In-phase changes of the IPO and AMO show a strengthened contribution to the regional and global OHC compared to the effect of either mode acting alone; the GMST increase (decrease) becomes more significant, as does the increase (decrease) in OHC in the upper 100-m OHC. Interaction between the IPO and AMO may be through a physical ocean process such as the AMOC, and also through an atmospheric bridge such as ENSO. Changes in AMOC strength influence ocean circulation and can affect the global redistribution of heat, leading to the influence of the AMO on the IPO. Changes in the phase of the IPO affect the frequency and magnitude of ENSO events, which in turn impact Atlantic surface temperature via the teleconnection of ENSO with midlatitude circulation patterns such as the Pacific–North America pattern and the North Atlantic Oscillation, and leading to the influence of the IPO on the AMO. For example, the positive heat anomaly in the upper 100-m layer in the Pacific weakens by about 25% with the inception of an in-phase IPO_AMO+ relative to the heat anomaly associated with the IPO+ alone, which is an indicator that a stronger AMOC pulls more heat from the Pacific into the Atlantic (Hu et al. 2010, 2012).

For completeness, we show the OHC anomaly in the deeper ocean in Figs. 3, 4, 7, and 8. With the exception of subpolar regions, the OHC anomalies in the deeper ocean are less significant and may represent the delayed imprint of the IPO and AMO; thus they are not discussed in any detail here.

6. Conclusions

We analyze the last 1000 years of the CESM Large Ensemble preindustrial control simulation to study the

relationship between decadal SST modes and OHC redistribution to show whether changes in these modes are related to global OHC redistribution. Specifically, we want to explore these relationships under constant background climate conditions to exclude the more complicated interactions between the internal climate modes and external forcings. The two leading decadal climate modes examined here are the interdecadal Pacific oscillation (IPO) and the Atlantic multidecadal oscillation (AMO).

Our analysis shows that the simulated IPO and AMO agree with observations reasonably well. Different phases of the IPO and AMO are correlated with the opposite sign of OHC anomalies in the upper 300-m ocean both globally and regionally, as do the global mean surface air temperature anomalies. For example, for the IPO+, the heat content in the surface layer (<100 m) and the global mean air temperature increase, whereas the heat content of the subsurface layer (100–300 m) decreases. The same is true in reverse for the IPO−. The underlying physical mechanisms are the IPO-related changes to surface winds and to STCs. For the AMO, the global mean OHC anomalies in the upper 300-m ocean have the same sign and are dominated by the changes to deep convection in the subpolar North Atlantic associated with AMOC. Regionally, the contribution of the IPO (AMO) to the global mean OHC anomaly appears to come mostly from the Pacific (Atlantic), and contributions of the IPO (AMO) to OHC anomalies in the ocean basins other than the Pacific (Atlantic) are less clear in this analysis. One possible reason for this is the delayed response of OHC to the IPO (AMO) in other ocean basins, especially in the deeper oceans.

Overall, the opposite sign of OHC anomalies between surface and subsurface ocean layers occurs mainly in the Pacific following a change of the IPO phase, but not the AMO phase, consistent with many previous studies (e.g., Meehl et al. 2011, 2013b, 2016; Kosaka and Xie 2013; England et al. 2014). Our study suggests that the recent global warming slowdown (hiatus) is primarily associated with the negative phase of the IPO, and the AMO may have played either no role or just a secondary role. This negative IPO and the associated changes in surface winds and STCs induce a redistribution of the heat absorbed by the ocean, leading to more heat being deposited into the subsurface ocean and slower surface warming. In future work, we will explore how external forcing and internal climate modes interact by using fully coupled twentieth- and twenty-first-century CESM large ensemble simulations together with single forcing simulations.

Acknowledgments. We thank Dr. Nan Rosenbloom for proofreading this manuscript. We also thank our three anonymous reviewers for their careful, insightful, and constructive comments that significantly improved this manuscript. This study was supported by the Regional and Global Climate Modelling Program (RGCM) of the U.S. Department of Energy's Office of Science (BER), Cooperative Agreement DE-FC02-97ER62402. Z. Hu and Y. Hu are supported by the National Natural Science Foundation of China under Grants 41375072 and 41530423. This research used computing resources of the Climate Simulation Laboratory at the National Center for Atmospheric Research (NCAR), which is sponsored by the National Science Foundation. The National Center for Atmospheric Research is sponsored by the National Science Foundation. We thank Warren G. Strand for his help with data processing.

REFERENCES

Booth, B. B. B., N. J. Dunstone, P. R. Halloran, T. Andrews, and N. Bellouin, 2012: Aerosols implicated as a prime driver of twentieth-century North Atlantic climate variability. *Nature*, **484**, 228–232, https://doi.org/10.1038/nature10946.

Bryan, F. O., N. Nakashiki, Y. Yoshida, and K. Maruyama, 2007: Response of the thermohaline circulation during different pathways toward greenhouse gas stabilization. *Ocean Circulation: Mechanisms and Impacts*, *Geophys. Monogr.*, Vol. 173, Amer. Geophys. Union, 351–365, https://doi.org/10.1029/GM173.

Buckley, M. W., and J. Marshall, 2016: Observations, inferences, and mechanisms of Atlantic meridional overturning circulation variability: A review. *Rev. Geophys.*, **54**, 5–63, https://doi.org/10.1002/2015RG000493.

Ceballos, L. I., E. Di Lorenzo, C. D. Hoyos, N. Schneider, and B. Taguchi, 2009: North Pacific Gyre Oscillation synchronizes climate fluctuations in the eastern and western boundary systems. *J. Climate*, **22**, 5163–5174, https://doi.org/10.1175/2009JCLI2848.1.

Chen, X., and K.-K. Tung, 2014: Varying planetary heat sink led to global-warming slowdown and acceleration. *Science*, **345**, 897–903, https://doi.org/10.1126/science.1254937.

——, and ——, 2016: Correspondence: Variations in ocean heat uptake during the surface warming hiatus. *Nat. Commun.*, **7**, 12541, https://doi.org/10.1038/ncomms12541.

Clement, A., K. Bellomo, L. N. Murphy, M. A. Cane, T. Mauritsen, G. Rädel, and B. Stevens, 2015: The Atlantic multidecadal oscillation without a role for ocean circulation. *Science*, **350**, 320–324, https://doi.org/10.1126/science.aab3980.

Dai, A., J. C. Fyfe, S.-P. Xie, and X. Dai, 2015: Decadal modulation of global surface temperature by internal climate variability. *Nat. Climate Change*, **5**, 555–559, https://doi.org/10.1038/nclimate2605.

Danabasoglu, G., 2008: On multidecadal variability of the Atlantic meridional overturning circulation in the Community Climate System Model version 3. *J. Climate*, **21**, 5524–5544, https://doi.org/10.1175/2008JCLI2019.1.

——, S. Bates, B. P. Briegleb, S. R. Jayne, M. Jochum, W. G. Large, S. Peacock, and S. G. Yeager, 2012a: The CCSM4 ocean

component. *J. Climate*, **25**, 1361–1389, https://doi.org/10.1175/JCLI-D-11-00091.1.

——, S. G. Yeager, Y.-O. Kwon, J. J. Tribbia, A. S. Phillips, and J. W. Hurrell, 2012b: Variability of the Atlantic meridional overturning circulation in CCSM4. *J. Climate*, **25**, 5153–5172, https://doi.org/10.1175/JCLI-D-11-00463.1.

Delworth, T. L., and M. E. Mann, 2000: Observed and simulated multidecadal variability in the Northern Hemisphere. *Climate Dyn.*, **16**, 661–676, https://doi.org/10.1007/s003820000075.

——, S. Manabe, and R. J. Stouffer, 1993: Interdecadal variations of the thermohaline circulation in a coupled ocean–atmosphere model. *J. Climate*, **6**, 1993–2011, https://doi.org/10.1175/1520-0442(1993)006<1993:IVOTTC>2.0.CO;2.

Deser, C., M. A. Alexander, S.-P. Xie, and A. S. Phillips, 2010: Sea surface temperature variability: Patterns and mechanisms. *Annu. Rev. Mar. Sci.*, **2**, 115–143, https://doi.org/10.1146/annurev-marine-120408-151453.

Dewar, W. K., 2001: On ocean dynamics in midlatitude climate. *J. Climate*, **14**, 4380–4397, https://doi.org/10.1175/1520-0442(2001)014<4380:OODIMC>2.0.CO;2.

England, M. H., and Coauthors, 2014: Recent intensification of wind-driven circulation in the Pacific and the ongoing warming hiatus. *Nat. Climate Change*, **4**, 222–227, https://doi.org/10.1038/nclimate2106.

Evan, A. T., D. J. Vimont, A. K. Heidinger, J. P. Kossin, and R. Bennartz, 2009: The role of aerosols in the evolution of tropical North Atlantic Ocean temperature anomalies. *Science*, **324**, 778–781, https://doi.org/10.1126/science.1167404.

Frankignoul, C., and K. Hasselmann, 1977: Stochastic climate models, Part II: Application to sea-surface temperature variability and thermocline variability. *Tellus*, **29**, 289–305, https://doi.org/10.3402/tellusa.v29i4.11362.

Fyfe, J. C., and Coauthors, 2016: Making sense of the early-2000s warming slowdown. *Nat. Climate Change*, **6**, 224–228, https://doi.org/10.1038/nclimate2938.

Gulev, S. K., M. Latif, N. Keenlyside, W. Park, and K. P. Koltermann, 2013: North Atlantic Ocean control on surface heat flux on multidecadal timescales. *Nature*, **499**, 464–467, https://doi.org/10.1038/nature12268.

Hansen, J., M. Sato, P. Kharecha, and K. von Schuckmann, 2011: Earth's energy imbalance and implications. *Atmos. Chem. Phys.*, **11**, 13 421–13 449, https://doi.org/10.5194/acp-11-13421-2011.

Hasselmann, K., 1976: Stochastic climate models. I: Theory. *Tellus*, **28**, 473–485, https://doi.org/10.3402/tellusa.v28i6.11316.

Hogg, A. M., P. D. Killworth, J. R. Blundell, and W. K. Dewar, 2005: Mechanisms of decadal variability of the wind-driven ocean circulation. *J. Phys. Oceanogr.*, **35**, 512–531, https://doi.org/10.1175/JPO2687.1.

Hu, A., and Coauthors, 2010: Influence of Bering Strait flow and North Atlantic circulation on glacial sea-level changes. *Nat. Geosci.*, **3**, 118–121, https://doi.org/10.1038/ngeo729.

——, G. A. Meehl, W. Han, and J. Yin, 2011: Effect of the potential melting of the Greenland Ice Sheet on the meridional overturning circulation and global climate in the future. *Deep-Sea Res. II*, **58**, 1914–1926, https://doi.org/10.1016/j.dsr2.2010.10.069.

——, and Coauthors, 2012: Role of the Bering Strait on the hysteresis of the ocean conveyor belt circulation and glacial climate stability. *Proc. Natl. Acad. Sci. USA*, **109**, 6417–6422, https://doi.org/10.1073/pnas.1116014109.

——, G. A. Meehl, W. Han, B. Otto-Bliesner, A. Abe-Ouchi, and N. Rosenbloom, 2015: Effects of the Bering Strait closure on AMOC and global climate under different background climates. *Prog. Oceanogr.*, **132**, 174–196, https://doi.org/10.1016/j.pocean.2014.02.004.

Hurrell, J. W., and Coauthors, 2013: The Community Earth System Model: A framework for collaborative research. *Bull. Amer. Meteor. Soc.*, **94**, 1339–1360, https://doi.org/10.1175/BAMS-D-12-00121.1.

Kaplan, A., M. A. Cane, Y. Kushnir, A. C. Clement, M. B. Blumenthal, and B. Rajagopalan, 1998: Analyses of global sea surface temperature 1856–1991. *J. Geophys. Res.*, **103**, 18 567–18 589, https://doi.org/10.1029/97JC01736.

Karl, T. R., and Coauthors, 2015: Possible artifacts of data biases in the recent global surface warming hiatus. *Science*, **348**, 1469–1472, https://doi.org/10.1126/science.aaa5632.

Kay, J. E., and Coauthors, 2015: The Community Earth System Model (CESM) large ensemble project: A community resource for studying climate change in the presence of internal climate variability. *Bull. Amer. Meteor. Soc.*, **96**, 1333–1349, https://doi.org/10.1175/BAMS-D-13-00255.1.

Knight, J. R., R. J. Allan, C. K. Folland, M. Vellinga, and M. E. Mann, 2005: A signature of persistent natural thermohaline circulation cycles in observed climate. *Geophys. Res. Lett.*, **32**, L20708, https://doi.org/10.1029/2005GL024233.

Kosaka, Y., and S.-P. Xie, 2013: Recent global-warming hiatus tied to equatorial Pacific surface cooling. *Nature*, **501**, 403–407, https://doi.org/10.1038/nature12534.

——, and ——, 2016: The tropical Pacific as a key pacemaker of the variable rates of global warming. *Nat. Geosci.*, **9**, 669–673, https://doi.org/10.1038/ngeo2770.

Latif, M., and T. P. Barnett, 1994: Causes of decadal climate variability over the North Pacific and North America. *Science*, **266**, 634–637, https://doi.org/10.1126/science.266.5185.634.

——, and ——, 1996: Decadal climate variability over the North Pacific and North America: Dynamics and predictability. *J. Climate*, **9**, 2407–2423, https://doi.org/10.1175/1520-0442(1996)009<2407:DCVOTN>2.0.CO;2.

——, and Coauthors, 2004: Reconstructing, monitoring, and predicting multidecadal-scale changes in the North Atlantic thermohaline circulation with sea surface temperature. *J. Climate*, **17**, 1605–1614, https://doi.org/10.1175/1520-0442(2004)017<1605:RMAPMC>2.0.CO;2.

Lee, S.-K., W. Park, M. O. Baringer, A. L. Gordon, B. Huber, and Y. Liu, 2015: Pacific origin of the abrupt increase in Indian Ocean heat content during the warming hiatus. *Nat. Geosci.*, **8**, 445–449, https://doi.org/10.1038/ngeo2438.

Lewandowsky, S., J. S. Risbey, and N. Oreskes, 2016: The "pause" in global warming. *Bull. Amer. Meteor. Soc.*, **97**, 723–733, https://doi.org/10.1175/BAMS-D-14-00106.1.

Liu, W., S.-P. Xie, and J. Lu, 2016a: Reply to: 'Correspondence: Variations in ocean heat uptake during the surface warming hiatus.' *Nat. Commun.*, **7**, 12 542, https://doi.org/10.1038/ncomms12542.

——, ——, and ——, 2016b: Tracking ocean heat uptake during the surface warming hiatus. *Nat. Commun.*, **7**, 10926, https://doi.org/10.1038/ncomms10926.

Mann, M. E., and K. A. Emanuel, 2006: Atlantic hurricane trends linked to climate change. *Eos, Trans. Amer. Geophys. Union*, **87**, 233–241, https://doi.org/10.1029/2006EO240001.

McCarthy, G. D., I. D. Heigh, J. J.-M. Hirschi, J. P. Crist, and D. A. Smeed, 2015: Ocean impact on decadal Atlantic climate variability revealed by sea-level observations. *Nature*, **521**, 508–510, https://doi.org/10.1038/nature14491.

McGregor, S., A. Timmermann, M. F. Stuecker, M. H. England, M. Merrifield, F.-F. Jin, and Y. Chikamoto, 2014: Recent

Walker circulation strengthening and Pacific cooling amplified by Atlantic warming. *Nat. Climate Change*, **4**, 888–892, https://doi.org/10.1038/nclimate2330.

McPhaden, M. J., and D. Zhang, 2002: Slowdown of the meridional overturning circulation in the upper Pacific Ocean. *Nature*, **415**, 603–608, https://doi.org/10.1038/415603a.

Meehl, G. A., and A. Hu, 2006: Megadroughts in the Indian monsoon region and southwest North America and a mechanism for associated multidecadal Pacific sea surface temperature anomalies. *J. Climate*, **19**, 1605–1623, https://doi.org/10.1175/JCLI3675.1.

——, J. M. Arblaster, and W. G. Strand, 1998: Global scale decadal climate variability. *Geophys. Res. Lett.*, **25**, 3983–3986, https://doi.org/10.1029/1998GL900088.

——, ——, J. T. Fasullo, A. Hu, and K. E. Trenberth, 2011: Model-based evidence of deep-ocean heat uptake during surface-temperature hiatus periods. *Nat. Climate Change*, **1**, 360–364, https://doi.org/10.1038/nclimate1229.

——, and Coauthors, 2013a: Climate change projections in CESM1(CAM5) compared to CCSM4. *J. Climate*, **26**, 6287–6308, https://doi.org/10.1175/JCLI-D-12-00572.1.

——, A. Hu, J. M. Arblaster, J. Fasullo, and K. E. Trenberth, 2013b: Externally forced and internally generated decadal climate variability associated with the interdecadal Pacific oscillation. *J. Climate*, **26**, 7298–7310, https://doi.org/10.1175/JCLI-D-12-00548.1.

——, ——, B. D. Santer, and S.-P. Xie, 2016: Contribution of the interdecadal Pacific oscillation to twentieth-century global surface temperature trends. *Nat. Climate Change*, **6**, 1005–1008, https://doi.org/10.1038/nclimate3107.

Neale, R. B., J. Richter, S. Park, P. H. Lauritzen, S. J. Vavrus, P. J. Rasch, and M. Zhang, 2013: The mean climate of the Community Atmosphere Model (CAM4) in forced SST and fully coupled experiments. *J. Climate*, **26**, 5150–5168, https://doi.org/10.1175/JCLI-D-12-00236.1.

Nieves, V., J. K. Willis, and W. C. Patzert, 2015: Recent hiatus caused by decadal shift in Indo-Pacific heating. *Science*, **349**, 532–535, https://doi.org/10.1126/science.aaa4521.

Palmer, M. D., D. J. McNeall, and N. J. Dunstone, 2011: Importance of the deep ocean for estimating decadal changes in Earth's radiation. *Geophys. Res. Lett.*, **38**, L13707, https://doi.org/10.1029/2011GL047835.

Power, S., T. Casey, C. Folland, A. Colman, and V. Mehta, 1999: Inter-decadal modulation of the impact of ENSO on Australia. *Climate Dyn.*, **15**, 319–324, https://doi.org/10.1007/s003820050284.

Qiu, B., 2003: Kuroshio Extension variability and forcing of the Pacific decadal oscillations: Responses and potential feedback. *J. Phys. Oceanogr.*, **33**, 2465–2482, https://doi.org/10.1175/2459.1.

——, N. Schneider, and S. Chen, 2007: Coupled decadal variability in the North Pacific: An observationally constrained idealized model. *J. Climate*, **20**, 3602–3620, https://doi.org/10.1175/JCLI4190.1.

Rayner, N. A., D. E. Parker, E. B. Horton, C. K. Folland, L. V. Alexander, D. P. Rowell, E. C. Kent, and A. Kaplan, 2003: Global analyses of sea surface temperature, sea ice, and night marine air temperature since the late nineteenth century. *J. Geophys. Res.*, **108**, 4407, https://doi.org/10.1029/2002JD002670.

Santer, B. D., and Coauthors, 2014: Volcanic contribution to decadal changes in tropospheric temperature. *Nat. Geosci.*, **7**, 185–189, https://doi.org/10.1038/ngeo2098.

Saravanan, R., and J. C. McWilliams, 1998: Advective ocean–atmosphere interaction: An analytical stochastic model with implications for decadal variability. *J. Climate*, **11**, 165–188, https://doi.org/10.1175/1520-0442(1998)011<0165:AOAIAA>2.0.CO;2.

Schneider, N., and B. D. Cornuelle, 2005: The forcing of the Pacific decadal oscillation. *J. Climate*, **18**, 4355–4373, https://doi.org/10.1175/JCLI3527.1.

Semenov, V. A., M. Latif, D. Dommenget, N. S. Keenlyside, A. Strehz, T. Martin, and W. Park, 2010: The impact of North Atlantic-Arctic multidecadal variability on Northern Hemisphere surface air temperature. *J. Climate*, **23**, 5668–5677, https://doi.org/10.1175/2010JCLI3347.1.

Si, D., and Y. Ding, 2016: Oceanic forcings of the interdecadal variability in East Asian summer rainfall. *J. Climate*, **29**, 7633–7649, https://doi.org/10.1175/JCLI-D-15-0792.1.

——, and A. Hu, 2017: Internally generated and externally forced multidecadal oceanic modes and their influence on the summer rainfall over East Asia. *J. Climate*, **30**, 8299–8316, https://doi.org/10.1175/JCLI-D-17-0065.1.

Smith, D. M., and Coauthors, 2016: Role of volcanic and anthropogenic aerosols in the recent global surface warming slowdown. *Nat. Climate Change*, **6**, 936–940, https://doi.org/10.1038/nclimate3058.

Taguchi, B., S.-P. Xie, H. Mitsudera, and A. Kubokawa, 2005: Response of the Kuroshio Extension to Rossby waves associated with the 1970s climate regime shift in a high-resolution ocean model. *J. Climate*, **18**, 2979–2995, https://doi.org/10.1175/JCLI3449.1.

Trenberth, K. E., J. T. Fasullo, and M. A. Balmaseda, 2014: Earth's energy imbalance. *J. Climate*, **27**, 3129–3144, https://doi.org/10.1175/JCLI-D-13-00294.1.

Weese, S. R., and F. O. Bryan, 2006: Climate impacts of systematic errors in the simulation of the path of the North Atlantic Current. *Geophys. Res. Lett.*, **33**, L19708, https://doi.org/10.1029/2006GL027669.

Yan, X.-H., T. Boyer, K. Trenberth, T. R. Karl, S.-P. Xie, V. Nieves, K.-K. Tung, and D. Roemmich, 2016: The global warming hiatus: Slowdown or redistribution? *Earth's Future*, **4**, 472–482, https://doi.org/10.1002/2016EF000417.

Zhang, R., and T. L. Delworth, 2006: Impact of Atlantic multidecadal oscillations on India/Sahel rainfall and Atlantic hurricanes. *Geophys. Res. Lett.*, **33**, L17712, https://doi.org/10.1029/2006GL026267.

——, and ——, 2007: Impact of the Atlantic multidecadal oscillation on North Pacific climate variability. *Geophys. Res. Lett.*, **34**, L23708, https://doi.org/10.1029/2007GL031601.

——, R. Sutton, G. Danabasoglu, T. L. Delworth, W. M. Kim, J. Robson, and S. G. Yeager, 2016: Comment on "The Atlantic multidecadal oscillation without a role for ocean circulation." *Science*, **352**, 1527, https://doi.org/10.1126/science.aaf1660.

Zhang, Y., J. M. Wallace, and D. S. Battisti, 1997: ENSO-like interdecadal variability: 1900–93. *J. Climate*, **10**, 1004–1020, https://doi.org/10.1175/1520-0442(1997)010<1004:ELIV>2.0.CO;2.